

- 1 Bedoya-Velásquez, A.E., Navas-Guzmán, F., de Arruda Moreira, G., Román, R., Cazorla,
- 2 A., Ortiz-Amezcu, P., Benavent-Oltra, J.A., Alados-Arboledas, L., Olmo-Reyes, F.J.,
- 3 Foyo-Moreno, I., Montilla-Rosero, E., Hoyos, C.D., Guerrero-Rascado, J.L.
- 4 Seasonal analysis of the atmosphere during five years by using microwave radiometry over
- 5 a mid-latitude site
- 6 (2019) Atmospheric Research, 218, pp. 78-89.
- 7 DOI: 10.1016/j.atmosres.2018.11.014

Seasonal analysis of the atmosphere during five years by using microwave radiometry over a mid-latitude site

Andrés Esteban Bedoya-Velásquez^{1,2,3}, Francisco Navas-Guzmán⁴, Gregori de Arruda Moreira^{1,2,6}, Roberto Román^{1,2,5}, Alberto Cazorla^{1,2}, Pablo Ortiz-Amezua^{1,2}, José Antonio Benavent-Oltra^{1,2}, Lucas Alados-Arboledas^{1,2}, Francisco José Olmo-Reyes^{1,2}, Inmaculada Foyo-Moreno^{1,2}, Elena Montilla-Rosero⁷, Carlos D. Hoyos⁸, and Juan Luis Guerrero-Rascado^{1,2}

¹Andalusian Institute for Earth System Research (IISTA-CEAMA), University of Granada, Autonomous Government of Andalusia, 18006, Granada, Spain.

²Department of Applied Physics, University of Granada. Granada, Spain.

³Facultad de Ciencias, Departamento de Física, Universidad Nacional de Colombia, Medellín, Colombia.

⁴Federal Office of Meteorology and Climatology MeteoSwiss, Payerne, Switzerland.

⁵Atmospheric Optics Group (GOA-UVa), Valladolid University, Valladolid, Spain.

⁶Institute of Research and Nuclear Energy, IPEN, São Paulo, Brazil.

⁷Physical Sciences Department, School of Science, EAFIT University, Medellín, Colombia.

⁸Facultad de Minas, Departamento de Geociencias y Medio Ambiente, Universidad Nacional de Colombia. Medellín, Colombia.

Correspondence to: Andrés Esteban Bedoya Velásquez (aebedoyav@correo.ugr.es)

Abstract

This work focuses on the analysis of the seasonal cycle of temperature and relative humidity (RH) profiles and integrated water vapor (IWV) obtained from microwave radiometer (MWR) measurements over the mid-latitude city of Granada, southern Spain. For completeness the study, the maximum atmospheric boundary layer height (ABLH^{max}) is also included. To this end, we have firstly characterized the HATPRO-RPG MWR errors using 55 co-located radiosondes (RS) by means of the mean-bias (\overline{bias}) profile and the standard deviation (SD_{bias}) profile classified under all-weather conditions and cloud-free conditions.

This characterization pointed out that temperature from HATPRO-MWR presents a very low \overline{bias} respects RS mostly below 2.0 km agl, ranging from positive to negative values under all-weather conditions (from 1.7 to -0.4 K with SD_{bias} up to 3.0 K). Under cloud-free conditions, the bias was very similar to that found under all-weather conditions (1.8 to -0.4 K) but with smaller SD_{bias} (up to 1.1 K). The same behavior is also seen in this lower part (ground to 2.0 km agl) for RH. Under all-weather conditions, the mean RH bias ranged from 3.0 to -4.0 % with SD_{bias} between 10 to 16.3 % while under cloud-free conditions the bias ranged from 2.0 to -0.4 % with SD_{bias} from 0.5 to 13.3 %. Above 2.0 km agl, the SD_{bias} error increases considerably up to 4 km agl (up to -20 %), and then decreases slightly above 7.0 km agl (up to -5 %). In addition, IWV values from MWR were also compared with the values obtained from the integration of RS profiles, showing a better linear fit under cloud-free conditions ($R^2=0.96$) than under all-weather conditions ($R^2=0.82$). The mean bias under cloud-free conditions was -0.80 kg/m² while for all-weather conditions it was -1.25 kg/m². Thus, the SD_{bias} for all the statistics (temperature, RH and IWV) of the comparison between MWR and RS presented higher values for all-

47 weather conditions than for cloud-free conditions ones. It points out that the presence of clouds is a key factor
48 to take into account when MWR products are used.

49 The second part of this work is devoted to a seasonal variability analysis over five years, leading us to
50 characterize thermodynamically the troposphere over our site. This city atmosphere presents a clear seasonal
51 cycle where temperature, $ABLH^{\max}$ and IWV increase from winter to summer and decrease in autumn,
52 meanwhile RH decreases along the warmer seasons. This city presents cold winters (mean daily maximum
53 temperature: 10.6 ± 1.1 °C) and dry/hot summers (mean daily maximum temperature of 28.8 ± 0.9 °C and mean
54 daily maximum of surface RH up to 55.0 ± 6.0 %) at surface (680 m asl). Moreover, considering temporal trends,
55 our study pointed out that only temperature and RH showed a linear increase in winters with a mean-rate of (0.5
56 ± 0.1) °C/year and (3.4 ± 1.7) %/year, respectively, from ground to 2.0 km agl, meanwhile IWV presented a
57 linear increase of $1.0 \text{ kg}\cdot\text{m}^{-2}/\text{year}$ in winters, $0.78 \text{ kg}\cdot\text{m}^{-2}/\text{year}$ in summers and a linear decrease in autumns of
58 $-0.75 \text{ kg}\cdot\text{m}^{-2}/\text{year}$.

59 KEYWORDS: Microwave radiometry, passive remote sensing, thermodynamic characterization of atmosphere,
60 atmospheric boundary layer.

61

62 **1 Introduction**

63 Tropospheric temperature and water vapor content are two key variables for understanding the thermodynamic
64 processes in the atmosphere. Firstly, the knowledge of the thermal structure in the lower part of the atmosphere
65 is a key input for atmospheric boundary layer (ABL) studies (Crook, 1996; Moreira et al., 2018), for turbulence
66 analysis (O'Connor et al., 2010; Vogelmann et al., 2012), regional climatology and mesoscale numerical models
67 applied on weather forecasting (Stevens and Bony, 2013). Secondly, the water vapor content is directly related
68 to the hydrological cycle, influencing the clouds formation and, therefore, the planetary albedo (Hoff and
69 Hardesty, 2012), and modifying the Earth energy balance at surface. Moreover, the water vapor contribution to
70 the natural greenhouse effect is up to 60 % under clear sky conditions, absorbing a significant part of the
71 outgoing infrared radiation (Kiehl and Trenberth, 1997), but also affecting the atmospheric chemical
72 composition and the atmospheric aerosol particles size (Boucher et al., 2013).

73

74 Radiosondes (RS) provide in-situ temperature and relative humidity (RH) measurements with high accuracy,
75 precision and vertical resolution. However, their applicability is constrained by several issues: (i) the low
76 frequency of launches; (ii) the air parcel probed might change because of the horizontal wind drift and variable
77 ascent rate during the measurement; (iii) the equipment and man-power costs; and (iv) limitations of
78 measurements under low relative humidity conditions (Vaughan et al., 1988). As an alternative, Raman lidar
79 (RL) systems, based on an active remote technique with high spatial and temporal resolution, can overcome
80 some of the RS drawbacks for measuring water vapor profiles. One of the disadvantages of Raman lidar systems
81 compared to RS is that weather conditions affect the measurements. Besides, these systems need to perform
82 regular calibrations of the water vapor Raman channel by using co-located RS or MWR (Mattis et al., 2002;

83 Guerrero-Rascado et al., 2008a; Navas-Guzmán et al., 2014, Bedoya-Velásquez, et al., 2018). In addition, due
84 to the low signal-to-noise-ratio inherent to the RL technique, it is mostly used during night-time. Other methods
85 to retrieve water vapour profiles are based on the synergy between in-situ aircraft and satellite measurements
86 (Stankov, 1998; Löhnert et al., 2004; Delanoe and Hogan, 2008).

87

88 Another approach for obtaining these atmospheric profiles is through passive remote sensing techniques. In this
89 sense, the MWR is an instrument that measures the thermal radiation emitted by the atmosphere within 20-200
90 GHz, operating in continuous mode (24/7) (Rose et al., 2005). Over other techniques, it can provide atmospheric
91 profiles with a high temporal resolution and a reasonable vertical resolution under almost all-weather conditions
92 (Navas-Guzmán et al., 2016). In addition to temperature and RH profiles, the MWR also provides integrated
93 quantities such as integrated water vapor (IWV) and liquid water path (LWP) with high accuracy (Crewell and
94 Löhnert, 2003; Löhnert and Crewell, 2003).

95

96 This work presents an analysis of the MWR performance in terms of accuracy and precision by means of a
97 comparison with RS measurements. The mean-bias (\overline{bias}) and the standard deviation (SD_{bias}) between MWR
98 and co-located RS have been calculated for the physical temperature and RH profiles, and for IWV. The study
99 also includes the investigation of the MWR performances under all-weather conditions versus cloud-free
100 conditions and daytime versus night-time measurements. After the characterization of the MWR performances,
101 we focused on a tropospheric analysis of the seasonal variability of temperature and RH profiles, IWV and the
102 atmospheric boundary layer height (ABLH) in the city of Granada, a Southern mid-latitude region in Spain,
103 over a period of five years.

104

105 The structure of the paper is described as follows. The experimental site and instrumentation is presented in
106 Section 2. Section 3 describes the methodology used to assess the MWR performance and to derive vertically-
107 resolved information on atmospheric thermodynamic properties and ABLH. In addition, it describes the data
108 pre-processing applied in the statistical seasonal study. Section 4 presents the results and discussion of the
109 comparison between MWR and RS measurements and the 5-year statistical analysis of thermodynamics profiles
110 over Granada. Finally, the conclusions are summarized in Section 5.

111

112 **2 Experimental site and instrumentation**

113 **2.1 Experimental site**

114 The data used in this work were collected at the urban station located in the IISTA-CEAMA building (Granada,
115 Spain, 37.16° N, 3.61° W, 680 m asl). The city is located in a natural basin surrounded by mountains with
116 elevations between 1000 and 3398 m above sea level (asl). Near continental conditions prevailing at this site
117 are responsible for large seasonal temperature differences, providing cool winters and hot summers. The diurnal
118 thermal oscillation at surface is quite high throughout the year, often reaching up to 20 °C, and relative humidity
119 is below 40% most of the time. The region is mostly affected in summer by mineral dust particles transported

120 from the North of Africa (Lyamani et al., 2006a, 2006b, 2010, 2012; Guerrero-Rascado et al., 2008b, 2009,
121 2011; Córdoba-Jabonero et al., 2011; Titos et al., 2012; Navas-Guzmán et al., 2013; Valenzuela et al., 2014;
122 Granados-Muñoz et al., 2016; Benavent-Oltra et al., 2017). Other aerosol sources are mainly produced by
123 traffic, domestic-heating (wintertime) and biomass burning transported from North America, North Africa and
124 the Iberian Peninsula itself (Alados-Arboledas et al., 2011; Navas-Guzmán et al., 2013; Ortiz-Amezcuca et al.,
125 2014, 2017; Titos et al., 2017).

126 **2.2 Instrumentation**

127 The main instrument used in this work is the ground-based MWR (RPG-HATPRO G2, Radiometer physics
128 GmbH) (Rose et al., 2005). This is a passive remote sensor, which measures the thermal emission of radiation
129 from the atmosphere in the microwave region. The MWR has a radiometric resolution between 0.3 and 0.4 rms
130 at 1.0-s integration time and a high temporal resolution for vertical profiles, retrieving roughly one profile each
131 two minutes. The MWR has two bands with seven channels each one, the K-band (22 - 31 GHz) provides
132 information about vertical humidity, making also possible to get information of integrated column products
133 such as IWV and LWP. The V-band (51 - 58 GHz) contains information about vertical temperature profile
134 (Löhnert and Mainer, 2012; Navas-Guzmán et al., 2016), associated to the thermal emission from molecular
135 oxygen in the atmosphere. Water vapor observations are performed at zenith position, while temperature
136 information can be retrieved assuming horizontal homogeneity and performing vertical scanning observations
137 (Löhnert et al., 2009). Vertical profiles of temperature and RH are composed by 39 bins, where 25 are below 2
138 km of altitude (roughly inside de ABL) with a variable resolution from 10 to 200 m. The vertical resolution in
139 the free troposphere (2 to 10 km) varies from 200 m to 2000 m (the last 14 bins). An absolute calibration is
140 recommended to be performed at least every 6 months, by using cold liquid-nitrogen and hot loads as reference
141 (Turner et al. 2007, Maschwitz et al., 2013). The accuracy of the temperature profile reported by the
142 manufacturer is lower than 0.75 K RMSE in the range 1.2 - 4.0 km and larger than 1.0 K RMSE from 4 to 10
143 km. However, there is no reported accuracy for RH profile, because RH profiles are retrieved from the
144 combination of temperature and absolute humidity profiles. The absolute humidity profiles have an accuracy
145 up to $\pm 0.02 \text{ g/m}^3$ RMS from 0 to 1 km, up to $\pm 0.04 \text{ g/m}^3$ RMS above 2 km), and within the boundary layer up
146 to $\pm 0.03 \text{ g/m}^3$ RMS (i.e. 0-2000 m). MWRs commonly use temperature inversion methods based on neural
147 networks or linear regressions, which requires a long database taken close to the instrument for training them
148 (Cimini, et al., 2015), normally, many RSs are used for this aim, becoming it their principal disadvantage. Also,
149 other inversion algorithms based on Optimal Estimation Method (Rodgers, 2000) have been used in the last
150 years to overcome this problem (Bernet et al., 2017; Navas-Guzmán et al., 2014b, 2017). In this work, the
151 manufacturer has performed the training of the MWR inversion algorithm by using neural networks.

152

153 RSs are launched from IISTA-CEAMA mainly during field campaigns or specifically for RL water vapor
154 channel calibration (Guerrero-Rascado et al., 2008a; Navas-Guzmán et al., 2014a; Granados-Muñoz et al.,
155 2015; Bedoya-Velásquez et al., 2018). The system used for RS launches is a GRAW DFM-06/09 (GRAW

156 Radiosondes, Germany), which provides profiles of temperature (resolution 0.01°K, accuracy 0.2 °K), pressure
 157 (resolution 0.1 hPa, accuracy 0.5 hPa) and RH (resolution 1%, accuracy 2%), with vertical resolution depending
 158 on the RS ascension velocity, usually around 5 m/s. Data acquisition done by a GRAWmet software and ground
 159 station are used. Up to 55 RSs were launched, mainly during summertime, during the five-year period analyzed
 160 here (2012 - 2016).

161

162 Additionally, a co-located Sun/sky photometer (Cimel Electronique; CE-318N) has been used in this study.
 163 This instrument belongs to AERONET (Holben et al., 1998), which processes the spectral Sun and sky
 164 measurements from the photometer and provides aerosol optical and microphysical properties integrated over
 165 the atmospheric column. Aerosol optical depth (AOD_λ) at 380, 440, 500, 675, 870 and 1020 nm are among the
 166 AERONET products (<https://aeronet.gsfc.nasa.gov>). The uncertainty in the retrieved AOD_λ , associated with
 167 primary calibration, is 0.01 for visible and infrared wavelengths, while the ultraviolet region has an uncertainty
 168 of 0.02 (Holben et al., 1998). In this work, water vapor product from AERONET (level 1.5; version 2) was used
 169 as $IWV_{aeronet}$.

170

171 Finally, in order to discern clear and cloudy conditions, we have used a cloud cover database obtained from the
 172 co-located sky cameras installed on the IISTA-CEAMA roof-top. Cloud cover information from January 2012
 173 to January 2015 was retrieved from the All Sky Imager shown in Cazorla et al. (2008) and Román et al. (2012);
 174 while from February 2015 to December 2016 cloud cover was obtained from the SONA sky camera presented
 175 in Cazorla et al. (2015) and Román et al. (2017b). A full description of both cameras and methods for each one
 176 can be found in Cazorla et al. (2008) and Román et al. (2017a).

177

178 **3 Methodology**

179 **3.1 Assessment of MWR versus RS**

180 In order to characterize the accuracy and precision of the physical temperature and RH profiles from the MWR,
 181 a statistical analysis based on the comparison with RS has been done. During this 5-year period, simultaneous
 182 measurements of RS and MWR were available, with a total of 55 RS launches of which 23 RS were launched
 183 under cloud-free conditions. Thus, the comparison was done by means of the \overline{bias} (Eq. 1), which was
 184 interpreted as the accuracy of the MWR measurements,

$$185 \quad \overline{bias}(z) = \frac{1}{N} [\sum_{i=1}^N (MWR_i(z) - RS_i(z))] \quad (1)$$

186 and the standard deviation (SD) (Eq. 2), that provided information about the precision of the MWR,

$$187 \quad SD_{bias}(z) = \sqrt{\frac{\sum_{i=1}^N (bias_i(z) - \overline{bias}(z))^2}{N-1}} \quad (2)$$

188 Where z is the altitude and N is the total data-samples. In order to perform the comparison between RS and
189 MWR profiles, all RS measurements were degraded to the MWR spatial resolution, which has a lower vertical
190 resolution, and the MWR profiles were 30 min-averaged after the RS launch time.

191 For analyzing the error in the IWV product of MWR, considering RS as reference, the relative mean-bias error
192 (MBE) calculation was performed, as follows:

$$193 \quad MBE = \frac{1}{N} \sum_{i=1}^N \frac{IWV_{MWR_i} - IWV_{RS_i}}{IWV_{RS_i}} \quad (3)$$

194 The criteria defined for classifying cloud-free conditions days was based on two flags. Firstly, we used the
195 cloud cover from sky camera database assuming cloud cover ≤ 1.0 oktas as cloud-free conditions. Secondly,
196 we defined a threshold by the observation of the LWP and by checking the cloud base height from MWR,
197 finding a representative threshold of LWP for cloud-free days $\leq 40 g/m^2$. In addition, we used the MWR rain
198 flag provided by the manufacturer to exclude rainy days from database.

199 The MWR performance for IWV was also characterized by means of the mean bias error and also calculating
200 the correlation between the IWV from MWR and the integration of the water vapor mixing ratio ($r(z)$) derived
201 by RS from 0 to 10 km (without degradation of spatial resolution of the RS). This evaluation was also performed
202 for cloud-free conditions and all-weather conditions classification.

203 A classification was performed only for cloud-free conditions between daytime and night-time, considering
204 daytime the measures which were obtained under sunlight presence and night-time measures under absence of
205 sunlight, according to the seasons, resulting in 11 comparison cases during daytime and 12 comparison cases
206 during night-time.

207

208 **3.2 Calculation of ABLH by using microwave radiometer**

209 The algorithm used for the ABLH determination using MWR measurements is described in detail in Moreira
210 et al. (2018). This algorithm combines two methodologies: the parcel method (PM) and the temperature gradient
211 method (TGM), which are based on the vertical temperature ($T(z)$) and potential temperature profiles ($\theta(z)$)
212 obtained from MWR by using the definition proposed in Stull, 2011.

213 Thus, the $\theta(z)$ was analyzed in order to classify the atmospheric conditions as stable or unstable. This analysis
214 was performed by the comparison of the surface potential temperature ($\theta(z_0)$) with all points in the $\theta(z)$ profile
215 below 5 km. The situation was classified as stable if all $\theta(z)$ data points had values larger than $\theta(z_0)$ and thus,
216 TGM is applied. Otherwise, the condition was classified as unstable and, therefore, PM is used.

217 The PM assumes the ABLH as the height z where the $\theta(z)$ is equal to surface potential $\theta(z_0)$, because z is the
218 altitude where an air parcel with ambient temperature (T) can rise adiabatically from the ground by convection

219 (Holzworth, 1964). Such method is applicable only under unstable situations, i.e. inside a convective boundary
220 layer.

221 The TGM (Stull, 1988) detects the ABLH in stable situations based on two definitions. Firstly, the surface-
222 based temperature inversion, meaning that TGM detects the first height z where T decrease as a function of
223 altitude. Secondly, the top of the stable boundary layer, meaning that TGM finds the first height where $d\theta/dz =$
224 0.

225 The first step is to detect the altitude z where the surface-base temperature inversion is situated (from T profile).
226 Then, from z is found the top of stable boundary layer in the $\theta(z)$. If surface-base temperature inversion or top
227 of stable boundary layer is not found, the ABLH is classified as “not identified”.

228 **3.3 Statistical seasonal study**

229 The total of measures performed are presented in table 1, reaching up around one of million profiles measured
230 with MWR over the whole five-years period, separating the calibration days and periods with data absence
231 mainly associated to maintenance of the instrument. For this seasonal statistical study, we defined the seasons
232 by months as follows: winter (December, January and February), spring (March, April and May), summer (June,
233 July and August) and autumn (September, October and November). Here, we performed an hourly-average for
234 each season of every year evaluated in order to have mean-seasonal-behavior from 0 to 24 hours to determine
235 the seasonal diurnal cycle (vertical behavior for temperature and RH, and columnar integrated behavior for
236 IWV), adding the results of the mean ABLH^{max}. Then, we divided the atmosphere in nine probed volumes: H1
237 (bins: 1-14, from 0 to 0.55 km agl), H2 (bins: 15-19, from 0.6 to 1.0 km agl), H3 (bins: 20-22, from 1.2 to 1.5
238 km agl), H4 (bins: 23-25, from 1.6 to 2.0 km agl), H5 (bins: 26-29, from 2.2 to 3.1 km agl), H6 (bins: 30-32,
239 from 3.5 to 4.4 km agl), H7 (bins: 33-35, from 5.0 to 6.2 km agl), H8 (bins: 36-37, from 7.0 to 8.0 km agl), H9
240 (bins: 38-39, from 9.0 to 10.0 km agl), in order to look for the seasonal variability of the median of the
241 temperature and RH within the different tropospheric regions. In addition, we also used the median-seasonal
242 trend of PW along the five years took from NASA AERONET level 1.5 level data for the Granada station to
243 support some of the results obtained.

244 **4 Results and discussion**

245 246 **4.1 Characterization of MWR performances versus RS**

247 Figure 1 presents the (\overline{bias} and SD_{bias}) between MWR radiometer and RS for temperature and relative humidity
248 under clear and all-weather conditions. These two statistic parameters are interpreted as the accuracy and the
249 precision, respectively, of the MWR measurements. Figure 1a shows high variability of the temperature \overline{bias}
250 for all-weather conditions mostly in the first hundreds of meters, passing from positive to negative values. The
251 larger deviations observed close to ground have been observed in similar comparisons for previous studies and
252 could be due to the larger uncertainties of the radiative transfer models for the most transparent MWR channels,
253 which affect more the temperature retrievals in the lowest layers (Navas-Guzmán et al. 2016). In general, below

254 2.0 km agl, the variability shows low-temperature \overline{bias} values from 1.7 to -0.4 K. The variability starts to
255 increase from negative to positive within 2.0 to 4.0 km agl (up to 1.0 K). This \overline{bias} increases up to 1.8 K above
256 4.0 km agl, indicating the losing of accuracy with altitude always with positive values. The SD_{bias} of the
257 temperature deviation profiles in all-weather conditions shows values lower than 3.0 K below 2.0 km agl,
258 increasing up to 3.2 K from 2.0 to 4.0 km agl, and keeping constant close to 3.0 K from 4 to 7 km agl. The
259 cloud-free conditions analysis shows the same variability in the mean bias within the first hundreds of meters
260 than the one observed for all-weather conditions, after this region the \overline{bias} changed from positive to negative
261 values, oscillating from 1.8 to -0.4 K (below 2.0 km agl). Then, between 2.0 to 4.0 km agl, the bias pass from
262 negative to positive. Above 4.0 km agl some variability lower than 1.7 K, indicating the losses of the accuracy
263 as altitude increases. The temperature SD_{bias} profile under cloud-free conditions presents values lower than 1.1
264 K from ground to 2.0 km agl, while they increase (up to 1.8 K) for higher altitudes. It is important to point out
265 the lower SD_{bias} values observed under cloud-free conditions, indicating a higher precision of temperature
266 MWR measurements under clear conditions than for all-weather conditions.

267 In addition, the surface heating caused by solar radiation tends to increase the variability of the temperature
268 profiles over the firsts kilometers of the troposphere (up to 3.0 km agl). Above this altitude the atmosphere
269 becomes cooler and the SD_{bias} profiles becomes quite constants.

270 The same analysis was performed for RH under all-weather conditions and cloud-free conditions (Fig 1.b).
271 Under all-weather conditions, the RH \overline{bias} profile shows relatively low deviations, passing from positive values
272 (from surface to 1.6 km agl) to negative (from 1.6 until 2.0 km agl) (from 3 to -4.0 %). The RH \overline{bias} becomes
273 greater (up to -18.0 %) from 2 to 4 km agl; then above 4 km agl reach up -11.0%. The SD_{bias} ranges from 10
274 to 16.3 % from ground to 2 km agl, above this altitude it presents a variation from 15 to 21.0 % (from 2 to 4
275 km agl). Then, it decrease from 4 to 7 km agl from 21 to 17 %. Cloud-free conditions \overline{bias} profile has a similar
276 behavior below 2 km agl (ranging from 2.0 to -4.0 %), then increasing up from -4.0 to -21.4 % until 4 km.
277 Finally, a decrease is seen to -4.5% from 4 to 7 km agl. Regarding SD_{bias} -RH profile in cloud-free conditions,
278 from ground to 2 km agl the discrepancy was ranging from 0.5 to 13.3 %, increasing from 2 to 3.0 km agl up to
279 19.3 %, then decreasing up to 15 % until 4.0 km agl. From 4.0 km agl to the top of the profile, decreasing until
280 9.3 %. This losing of precision, mostly between 2 to 4 km agl, might be associated to the method for retrieving
281 the RH profiles. This type of profile lose accuracy above the ABL, mainly because at this altitudes the absolute
282 humidity is typically quite low (due to the low temperatures) becoming very difficult a proper detection of this
283 property by microwave radiometry and, therefore, the RH retrievals loose precision. The SD_{Bias} -RH profile of
284 all-weather conditions presents higher variability respect to cloud-free conditions, showing a difference around
285 5 % over almost all the profile, which might be associated to the cloud presence.

286 Summarizing this inter-comparison, it is worth to point out that temperature profiles obtained from MWR makes
287 an underestimation of those taken by RS just between 1.5 to 2.3 km agl, the profile below 1.5 and above 2.3 km
288 agl presented an overestimation. The RH \overline{bias} profile exhibits an overestimation below 1.5 km agl, but above
289 this altitude, an underestimation of the RH profiles is seen from MWR respect to the obtained for RS.

290 In order to characterize the performance of MWR to retrieve IWV (IWV_{MWR}), an integration of the $r(z)$ profile
291 calculated from RS was performed to derive IWV_{RS} . Figure 2 shows the scatter plot between IWV_{MWR} and
292 IWV_{RS} . The fit for cloud-free conditions shows a slope closer to one (0.85 ± 0.03) and a better determination
293 coefficient ($R^2_{CFC} = 0.96$) than all-weather conditions (slope = 0.68 ± 0.03 , $R^2_{AWC} = 0.82$), which determines that
294 cloud-free days fit better. This fact is associated to the vertical and horizontal homogeneity that atmosphere
295 presents under cloud-free conditions, which is not seen for RS and MWR measurements under cloud presence,
296 evidencing high data dispersion in all-weather conditions (moving away to the 1:1 line). The MBE is also
297 calculated to reinforce the fact that all-weather conditions introduce large errors respect to cloud-free conditions
298 measurements, showing a MBE to cloud-free conditions up to -0.80 kg/m^2 , meanwhile for all-weather
299 conditions the MBE is up to -1.25 kg/m^2 . As seen in Fig 2, the cloud presence introduces high data-dispersion,
300 weakening the correlation.

301 The performance of the MWR has also been analyzed distinguishing between daytime and night-time
302 measurements (Fig.3), but only for cloud-free conditions since it is the scenario with better performance. The
303 temperature \overline{bias} is up to 2.0 K reached in the first hundreds of meters, which is the region with higher
304 variability. Above that, a positive temperature \overline{bias} is observed below 1.8 km agl, ranging from 0.7 to 1.0 K for
305 daytime and from 0.5 to 0.6 K until 1.5 km agl for night-time, showing lower variability during night-time
306 because of the sunlight absence. The \overline{bias} becomes negative from 1.8 to 3.5 km agl (up to -0.5 K) for daytime
307 and from 1.5 to 2.3 km agl (up to -0.5 K) to night-time. The \overline{bias} becomes positive above 3.5 km agl reaching
308 1.7 K for daytime and 1.8 K above 2.3 km agl for night-time. The SD_{bias} analyzed under the same three ranges
309 of altitude, presented lower values for daytime close to 0.6 K, 1.3 K and 1.7 K than night-time 1.0 K, 1.2 K and
310 2.0 K, in fact the night-time is relatively more variable under the first 2 km agl, maybe associated to the thermal
311 inversions during the night.

312 The same behavior is also seen on RH \overline{bias} -profile where the daytime profile is more variable within the first
313 1.5 km agl (up to 8 %) than night-time one (up to 2 %), which is almost constant in the first 1.5 km. The
314 variability at daytime is mostly associated to the Sun presence, because the temperature modifies the water
315 vapor pressure. From this altitude until 4.5 km agl for daytime and 5.5 km agl at night-time, the RH \overline{bias}
316 becomes negative decreasing up to -26.5% and -16.8% , respectively. From 4.5 to 7 km agl for daytime and
317 night-time from 5.5 to 7 km agl, the RH mean-bias decreased to -8.1% and -8.4% , respectively. $RH-SD_{bias}$
318 presented the following values according to the altitude ranges exposed above, for daytime from 6 to 8.8% (up
319 to 1.5 km agl), up to 23.5% (up to 4.5 km agl) and decreasing to 18.3 % (up to 7 km agl), while night-time
320 variates from 5 to 10.0% (within 1.5 km agl), increasing to 20.0 % (up to 4.5 km agl) and it starts to descend
321 up to 11.1% at 7.0 km agl. From this analysis, we can point out that the MWR present quite good performance
322 for RH in the first two kilometers, with mean bias and SD_{bias} lower than 10%. Above 2 km (agl) these profiles
323 should be used more carefully, taking into account that error might be as high as 20 %, affecting strongly the
324 calculations performed.

325

326 4.2 Statistical analysis of five-year of MWR measurements

327 4.2.1 Diurnal cycle analysis

328 In order to investigate the diurnal cycle of the temperature and RH profiles in the troposphere, the hourly-mean
329 cycle for temperature and RH profiles is analyzed for each season and every year from 2012 to 2016 (Fig.4 and
330 Fig. 5, respectively). To complete the study, ABLH^{max} retrievals have been included. Figure 4 shows the hourly-
331 mean behavior of the temperature profiles, where we can see that the maximum effect of the solar irradiation at
332 surface level is close to 16 UTC and the minimum around 7 UTC, varying slightly depending of the season.
333 In addition, due to the solar heating of the surface, the lowermost troposphere is heated with a variable vertical
334 extension, reaching up to 6 km agl in summer, and up to 5 km agl in autumn, becoming lower in winter (up to
335 2 km agl) and spring (up to 4 km agl). This effect mainly drives the evolution of the mean-ABLH, which is a
336 crucial parameter for studying aerosol dynamics and air masses transport (Moreira et al., 2018a,b).

337 The algorithm implemented for ABLH retrieval presented in Sec. 3.2 allows us to retrieve the altitude where
338 temperature profile evidences an abrupt change under stable or unstable atmospheric conditions. Thus, the
339 mean-ABLH^{max} presented on Fig. 4, increases gradually from winter (~ 2.1 km agl) to summer (~ 3.7 km agl),
340 because of the increasing in solar incoming radiation that reaches the Earth's surface. In autumn, the mean-
341 ABLH^{max} starts to decrease (~ 2.2 km agl), in agreement with the ABL studies reported by Moreira et al. (2018b)
342 over this area. ABLH^{max} starts to increase lately in the morning in winter (~ 7 UTC), meanwhile summer
343 exhibits faster increase up from 6 UTC, associated to the incoming solar insolation that begins earlier to warm
344 up the surface.

345 Fig. 4 determines that the warmest year of this study was 2015, with mean values at 16 UTC up to 11.6 ± 4.0
346 °C, 19.0 ± 4.1 °C and 30.0 ± 1.8 °C at surface level in winter, spring and summer, respectively. Autumn was
347 an exception, becoming autumn 2013 the warmest in the period 2012-2016, with mean-maximum temperature
348 of 23.1 ± 5.7 °C. The coldest mean values at ground level by season were reached in winter 2012 (10.5 ± 3.5
349 °C), spring 2013 (15.6 ± 7.6 °C), summer 2013 (27.5 ± 2.1 °C) and autumn 2012 (19.2 ± 6.4 °C).

350 Fig. 5 presents the same analysis for RH, where the hourly-mean maximum values for the RH profile at surface
351 level are observed close to 7 UTC. This is consistent with the lower temperature values, since the diurnal cycle
352 between temperature and RH is opposite. The intervals with higher RH are in late night and mornings (from 2
353 to 10 UTC) and night (from 21 to 24 UTC), where solar heating is weaker or absent. In the mornings, RH
354 presents high values at surface level (winter ~ 80 %, spring ~ 65 %, summer ~ 50 % and autumn ~ 62 %). These
355 values tend to increase with altitude until 4 km agl in winter, spring and autumn, but in summer reaches up to
356 3 km because of higher temperatures. In the late afternoons, this value may be little lower at surface reaching
357 up in winter ~ 70 %, spring ~ 55 %, summer ~ 40 % and autumn ~ 60 %, experimenting the same increase with
358 altitude until 4 km agl depending of the season. The driest region observed in the RH profiles at surface level
359 is close to 16 UTC, and it reaches in winter ~ 60 %, spring ~ 48 %, summer ~ 28 % and autumn ~ 35 %. This
360 region can reach 5 km agl or more in spring and summer becoming lower in winter and autumn. As we shown

361 in Section 4.1, the RH mean-bias profiles above 2 km agl, losses accuracy and precision, therefore the results
362 above this altitude have larger uncertainties.

363 From Figs. 4 and 5, it is detected a clear seasonal cycle in temperature, RH and $ABLH^{max}$, governed by solar
364 radiation. Granada is characterized by cold winters (mean hourly maximum temperature at surface of $10.6 \pm$
365 1.1 °C) and warmer summers (mean-hourly maximum of 28.8 ± 0.9 °C). In summer, RH at surface can be as
366 low as 18.5 ± 1.9 % (mean-hourly minimum value) in the driest part of the day and in the mornings where
367 humidity is higher; it could reach a mean-hourly maximum of 55 ± 6 %, evidencing the dry conditions of this
368 city.

369 **4.2.2 Statistical analysis of temperature and RH in the vertical coordinate**

370 In this section, a seasonal variability study of atmospheric variables like temperature and RH in altitude and
371 IWV in column is presented. Figure 6 shows the temperature boxplots by year and season. In addition, we
372 divided the profile by nine bins to cover the whole troposphere as was describe in section 3.3, allowing us to
373 investigate effects inside the low troposphere, which is directly linked with ABL (typically from 0 to 3 km agl)
374 and middle and high troposphere (from 3km agl to 10 km agl). Accordingly, to the results obtained in sec. 4.2.1,
375 we are only interested on studying when temperature exhibits their maximum value along the day over all
376 seasons (RH behaves oppositely); therefore, this statistical analysis will be performed at 16 UTC. Around this
377 hour, the ABL is fully developed and the atmosphere is good mixed.

378 Temperature boxplots dataset shows that 25 % of the lowest and 25% of the highest temperatures are
379 symmetrically distributed respect to the median value showing low data dispersion for most of height-ranges
380 evaluated. In general, all seasons presented in 2013 smaller boxes than the other seasons, mostly between H1
381 to H4. Figure 6 presents that outliers are more frequent within H1 to H5, increasing in summer, associated to
382 the increase of the variability caused by high temperatures within ABLH.

383 RH boxes (Fig. 7) are quite larger than temperature pointing a higher data dispersion. In addition, RH shows
384 much more outliers (both above and below the boxes), mainly associated to (i) the cloud presence and (ii) the
385 decrease of the absolute humidity with altitude, making less accurate the radiometric measures. This fact makes
386 that MWR retrievals present higher or lower values than real measurements above 2.0 km agl, producing more
387 outliers. RH presents a trend to increase from H1 to H3 and decreasing from H4 to H9 for winter, spring and
388 autumn. This trend is broke up in summer when this increase reaches higher altitudes (from H1 to H6), and
389 decreases from H7 to H9.

390 In general, IWV data boxplots presented in Fig. 8 exhibit less data-dispersion. The distribution of the data shows
391 high equilibrium below 25 % and above 75 %, meaning that values are relatively well distributed around the
392 median with lower data outliers. This variable presents a seasonal trend to increase from winter to summer and
393 decreasing in autumn, showing their high relation with temperature seasonal trend.

394

395 4.2.3 Inter-annual trend analysis by season

396 Table 2 reports for each season the inter-annual trend of temperature and RH computed by means of the
397 calculation of the linear fits of the median values registered. Temperature only exhibits an inter-annual increase
398 from H1 to H7 in winter season, from 0 to 1.0 km agl, increased between 0.4 and 0.6 °C/year, depending on the
399 height range. Thus, winters in Granada are becoming warmer, mostly within the first 2.0 km agl. With a weaker
400 correlation ($R^2=0.44$), summers exhibit an increase of 0.4 °C/year only close to surface (H1). The rest of the
401 seasons do not present a clear inter-annual trend, with determination of R^2 coefficients below 0.50 for all height-
402 ranges.

403 The results of the inter-annual increase of temperature are in agreement with climatological studies performed
404 at Iberian Peninsula by Río et al. (2011) and Coll et al. (2017), reporting a surface temperature increasing trend
405 in winter in the South and South-Eastern of the peninsula, where Granada station presented the drier conditions
406 in the southern region of the peninsula. The results obtained here presents higher values for the inter-annual
407 trend of temperature respect to those reported in literature, mainly because the instrumentation involved, the
408 dataset size and the statistical techniques used in the datasets. Moreover, the inter-annual temperature increases
409 in winter season reported in this study are also in agreement to the report of CALIMA (Caracterización de
410 Aerosoles originados por Intrusiones de Masas de aire Africanas, *characterization of African air masses*
411 *outbreaks*, <http://www.calima.ws/episodiosocurridos.html>), which is a program in charge to quantify the
412 Saharan dust events over Iberian Peninsula. Its record indicates that from 2013 to 2015 the Saharan dust
413 outbreaks have increased their number and become more intense in winter season, mostly within the second
414 fortnight of February.

415 Regarding RH, winter presents a clearly linear increase for all the altitudes analyzed (note that information at
416 ranges H6-H9 are not included due to the loose of accuracy and precision of the RH retrievals following section
417 4.1). The highest rates of increasing are in the middle of the troposphere (between H4 and H5, 7.4 and 5.4
418 %/year, respectively). In spring, the RH increases linearly from H2 to H4. In summer and autumn, non-
419 significant inter-annual trend were observed.

420 Table 3 presents the inter-annual trend of IWV and PW by season. Our computations indicate that IWV is
421 increasing over the years with high correlations in winter ($1.0 \pm 0.1 \text{kgm}^{-2}/\text{year}$, $R^2=0.95$) and summer ($0.8 \pm$
422 $0.1 \text{kgm}^{-2}/\text{year}$, $R^2=0.73$), while PW only experimented an increasing trend high correlated ($0.07 \pm 0.03 \text{cm}/\text{year}$,
423 $R^2=0.6$) in winter. This behavior in winter pointed out that every year during our study Granada is becoming
424 more humid; furthermore, the likelihood of precipitations is higher in winter than in the rest of seasons. The
425 IWV in spring presented no-correlation (up to 0.26) due to the higher median value found in 2016 (up to 12.5
426 kgm^{-2}), this value tends to change the real tendency to decrease of this season (also seen in Fig. 8). If we perform
427 the analysis hiding spring 2016 median data, IWV in spring presents a decreasing tendency with a slope up to
428 $-0.2 \text{kgm}^{-2}/\text{year}$ and $R^2=0.80$. The fact of IWV in 2016 becomes higher is not clearly seen in this study, just we
429 could associate to the statistical weight, because in March the percentage of missing data is up to 64.5 % (11
430 days measured), so the median value of the month could affect the seasonal median. IWV in autumn presented

431 a strong correlation ($R^2=0.95$) with a linear decrease up to $-0.75 \text{ kgm}^{-2}/\text{year}$ which is not really linked with
432 inter-annual temperature cycle. This analysis showed no-correlation of PW in spring, summer and autumn,
433 however the seasonal trends for both IWV and PW are the same, increasing from winter to summer and
434 decreasing in autumn. The higher values of IWV were reached in spring and summer, mostly associated to the
435 vegetation presence and high temperatures, which increases the evapotranspiration process. Finally, it is
436 important to taking into account the warm air masses that comes from Atlantic Ocean and Mediterranean Sea,
437 with high temperatures, this fact increase the capacity of these air masses to harbor water vapor before
438 saturation.

439 5 Conclusions

440 Our analysis over a 5-year dataset of the RPG-HATPRO MWR led us to quantify its accuracy and precision
441 by means of the mean-bias and standard deviation for temperature and RH vertical profiles under cloud-free
442 conditions and all-weather condition, and integrated water vapor (IWV) column product. In addition, an
443 analysis of the MWR performances during night- and day-time was carried out under cloud-free conditions.
444 We found that the temperature \overline{bias} profile under all-weather conditions exhibited high confidence, mostly
445 below 2 km agl with values ranging from 1.7 to -0.4K . The SD_{bias} under all-weather conditions was quite
446 constant in altitude, with values around 3 K in the whole troposphere. Under cloud-free conditions, the mean
447 bias showed quite similar values than under all-weather conditions, although some differences were found in
448 the lowest layer (below 1.5 km) and between 3 and 5 km (agl), where the mean bias was slightly higher under
449 cloud-free conditions reaching up to 1.8 K. An important point to be remarked is the lower SD_{bias} that was
450 observed under cloud-free conditions. The SD_{bias} profile presented values ranging between 1.1 and 1.8 K in
451 the whole troposphere, indicating a higher precision of the MWR under these conditions.

452 The performance for RH under all-weather conditions showed from surface to 2 km agl that \overline{bias} was ranging
453 from 3.0 to -4.0% with SD_{bias} between 10 to 16.3 %, and from 2 to 4 km the \overline{bias} was up to -18% with SD_{bias}
454 ranging between 15 to 21 %. Above 4 km the \overline{bias} reached up to -11.0 with SD_{bias} ranging from 12 to 17 %.
455 The same altitudes ranges were evaluated under cloud-free conditions showed high confidence within the first
456 2 km ranging from 2.0 to -0.4 with SD_{bias} from 0.5 to 13.3 %, then from 2 to 3 km agl were up to -4.0 to -21.4
457 with SD_{bias} 19.3 %, and decreasing up to -4.5% with SD_{bias} 9.3 %. The temperature and RH SD_{bias} showed a
458 positive offset close to 2.5 K and 5 %, respectively, between all-weather conditions and cloud-free conditions,
459 associated with cloud presence. Finally, a performance of the IWV product allowed us to see the effect of the
460 cloud presence over this product. Thus, the determination coefficient was up to 0.82 for all-weather conditions,
461 meanwhile it increases up to 0.96 under cloud-free conditions. The MBE was lower for all-weather conditions ($-$
462 0.80 kg/m^2) than cloud-free conditions (-1.25 kg/m^2).

463 The cloud-free conditions database (temperature and RH) was investigated under daytime and night-time
464 scenarios. This classification exhibits a time-dependency associated to the solar heating on the surface,
465 becoming more variable during daytime respect to night-time. The temperature \overline{bias} profile was ranging from
466 0.7 and 1.0 K with SD_{bias} up to 1.0 K agl at daytime below 1.8 km agl and from 0.5 to 0.6 K at night-time with

467 SD_{Bias} 0.6 K below 1.5 km. This error increase with altitude. The RH also presents low errors below 1.5 km agl
468 up to 8 % at daytime with SD_{bias} ranging from 6 to 8.8 % and up to 2 % with SD_{bias} ranging from 5 to 10 % at
469 night-time. After this altitude, the accuracy and precision increase rapidly with height.

470 The results obtained here allows to assess the reliability range of the HATPRO MWR G2 system, in order to
471 use products like temperature, RH and IWV in further applications like foresting models, ABL studies, and
472 aerosol hygroscopic growth, among others at this mid-latitude region.

473 The second part of this work was focused on a statistical study over a 5-year dataset. Firstly, it was observed
474 that temperature, IWV and ABLH^{max} daily-seasonal cycle presents an increasing trend from winter to summer,
475 decreasing in autumn, meanwhile RH daily-seasonal cycle is opposite, maximum in winter decreasing until
476 summer and then increasing again in autumn; all of them governed by the solar radiation. The maximum
477 temperature values were around 16 UTC coinciding with the minimums RH values, instead RH maximums are
478 located from 2 to 10 UTC and from 21 to 24 UTC. The hourly- mean cycle leading us to conclude that 2015
479 was the warmest year for all seasons, except in autumn 2013 that showed up an abruptly increase of temperature
480 respect to other years. The coldest seasons do not follow a yearly pattern, becoming the coldest winter 2012,
481 spring 2014, summer 2014 and autumn 2015. The highest RH values were found in winter 2016, spring 2016,
482 summer 2015 and autumn 2016; and the lowest RH values in winter 2012, spring 2014, summer 2014 and
483 autumn 2014. Finally, the inter-annual study is linked with seasonal, pointing out that temperature and RH
484 showed up an inter-annual linear increase in winter with a mean-trend up to $(0.5 \pm 0.1) ^\circ\text{C}/\text{year}$ and (3.4 ± 1.7)
485 $\%/\text{year}$, respectively, from ground to 6 km agl. IWV presented an inter-annual linear increase up to 1 kgm^{-2}
486 $/\text{year}$ in winter and $0.78 \text{ kgm}^{-2}/\text{year}$ in summer. The autumn presents a linear decrease trend up to -0.75 kgm^{-2}
487 $/\text{year}$.

488 This work will provide solid ancillary information for ongoing investigations on topics such as aerosol
489 hygroscopic growth, forecast models, aerosol transport and ABLH calculations over this region by using MWR
490 products.

491

492 **Acknowledgments**

493 This work was supported by the Andalusia Regional Government through project P12-RNM-2409; by the
494 Spanish Ministry of Economy and Competitiveness through projects CGL2013-45410-R, CGL2015-73250-JIN
495 and CGL2016-81092-R, the Excellence network CGL2017-90884-REDT, the FPI grant (BES-2014- 068893),
496 and the Juan de la Cierva grant IJCI-2016-30007; by the University of Granada trough the Plan Propio Program
497 P9 Call-2013 contract and the project UCE-PP2017. Andrés Bedoya has been supported by a grant for PhD
498 studies in Colombia, COLCIENCIAS (Doctorado Nacional – 647), associated with the Physics Sciences
499 program at the Universidad Nacional de Colombia, Sede Medellín and by the Asociación Universitaria
500 Iberoamericana de Postgrado (AUIP). The study has also been supported by the Swiss National Science
501 Foundation trough project PZ00P2_168114. Financial support for EARLINET was through the ACTRIS

502 Research Infrastructure Project EU H2020 (Grant agreement no. 654109), particularly through the TNA GRA-3
503 HYGROLIRA. The authors gratefully acknowledge the FEDER program for the instrumentation used in this
504 work

505 **References**

506 Alados-Arboledas, L., Müller, D., Guerrero-Rascado, J., Navas-Guzmán, F., Pérez-Ramírez, D., and Olmo, F.:
507 Optical and microphysical properties of fresh biomass burning aerosol retrieved by Raman lidar, and star-and
508 sun-photometry, *Geophys. Res. Lett.* 38, L01807, doi: 10.1029/2010GL045999, 2011.

509

510 Bedoya-Velásquez, A. E., Navas-Guzmán, F., Granados-Muñoz, M. J., Titos, G., Román, R., Casquero-Vera,
511 J. A., Ortiz-Amezcuca, P., Benavent-Oltra, J. A., de Arruda Moreira, G., Montilla-Rosero, E., Hoyos, C. D.,
512 Artiñano, B., Coz, E., Olmo-Reyes, F. J., Alados-Arboledas, L., and Guerrero-Rascado, J. L.: Hygroscopic
513 growth study in the framework of EARLINET during the SLOPE I campaign: synergy of remote sensing and
514 in situ instrumentation, *Atmos. Chem. Phys.*, 18, 7001-7017, <https://doi.org/10.5194/acp-18-7001-2018>, 2018.

515 Benavent-Oltra, J. A., Román, R., Granados-Muñoz, M. J., Pérez-Ramírez, D., Ortiz-Amezcuca, P., Denjean,
516 C., Lopatin, A., Lyamani, H., Torres, B., Guerrero-Rascado, J. L., Fuertes, D., Dubovik, O., Chaikovsky, A.,
517 Olmo, F. J., Mallet, M., and Alados-Arboledas, L.: Comparative assessment of GRASP algorithm for a dust
518 event over Granada (Spain) during ChArMEx-ADRIMED 2013 campaign, *Atmos. Meas. Tech.*, 10, 4439-
519 4457, <https://doi.org/10.5194/amt-10-4439-2017>, 2017.

520

521 Bernet, L., F. Navas-Guzmán and N. Kampfer: The effect of cloud liquid water on tropospheric temperature
522 retrievals from microwave measurements, *Atmos. Meas. Tech.*, 10, 442-4437, [https://doi.org/10.5194/amt-10-](https://doi.org/10.5194/amt-10-4421-2017)
523 4421-2017, 2017.

524

525 Boucher, O., Randall, D., Artaxo, P., Bretherton, C., Feingold, G., Forster, P., Kerminen, V.-M., Kondo, Y.,
526 Liao, H., Lohmann, U., Rasch, P., Satheesh, S. K., Sherwood, S., Stevens, B., and Zhang, X. Y.: Clouds and
527 Aerosols, in: *Climate Change 2013: The Physical Science Basis. Contribution of Working Group I to the Fifth*
528 *Assessment Report of the Intergovernmental Panel on Climate Change*, edited by: Stocker, T. F., Qin, D.,
529 Plattner, G.-K., Tignor, M., Allen, S. K., Boschung, J., Nauels, A., Xia, Y., Bex, V., and Midgley, P. M.,
530 Cambridge University Press, Cambridge, UK and New York, NY, USA, 2013.

531

532 Cazorla, A., Casquero-Vera, J. A., Román, R., Guerrero-Rascado, J. L., Toledano, C., Cachorro, V. E., Orza, J.
533 A. G., Cancillo, M. L., Serrano, A., Titos, G., Pandolfi, M., Alastuey, A., Hanrieder, N., and Alados-Arboledas,
534 L.: Near-real-time processing of a ceilometer network assisted with sun-photometer data: monitoring a dust
535 outbreak over the Iberian Peninsula, *Atmos. Chem. Phys.*, 17, 11861-11876, [https://doi.org/10.5194/acp-17-](https://doi.org/10.5194/acp-17-11861-2017)
536 11861-2017, 2017.

537

538 Cazorla, A., Husillos, C., Antón, M., Alados-Arboledas, L.: Multi-exposure adaptive threshold technique for
539 cloud detection with sky imagers. *Sol. Energy* 114, 268–277, 2015

540

541 Cazorla, A., Olmo, F.J., Alados-Arboledas, L.: Development of a sky imager for cloud cover assessment. *Opt.*
542 *Soc. Am. A.*, vol 25, No. 1, 2008.

543 Cimini, D., Nelson, M., Güldner, J., and Ware, R.: Forecast indices from a ground-based microwave radiometer
544 for operational meteorology, *Atmos. Meas. Tech.*, 8, 315-333, <https://doi.org/10.5194/amt-8-315-2015>, 2015.

545 Coll, J., Aguilar, E. & Ashcroft, L.: Drought variability and change across the Iberian Peninsula.
546 *TheorApplClimatol* 130: 901. <https://doi.org/10.1007/s00704-016-1926-3>, 2017.

547 Cordell, R.L., Mazet, M., Dechoux, C., Hama, S.M.L., Staelens, J., Hofman, J., Stroobants, C., Roekens, E.,
548 Kos, G.P.A., Weijers, E.P., Frumau, K.F.A., Panteliadis, P., Delaunay, T., Wyche, K.P., Monks, P.S.:
549 Evaluation of biomass burning across North West Europe and its impact on air quality, *Atmospheric*
550 *Environment*, Volume 141, Pages 276-286, <https://doi.org/10.1016/j.atmosenv.2016.06.065>, 2016.

551 Córdoba-Jabonero, C., Sorribas, M., Guerrero-Rascado, J.L., Adame, J.A., Hernández, Y., Lyamani, H.,
552 Cachorro, V., Gil, M., Alados-Arboledas, L., Cuevas, E., De La Morena, B.: Synergetic monitoring of Saharan
553 dust plumes and potential impact on surface: A case study of dust transport from Canary Islands to Iberian
554 Peninsula. *Atmospheric Chemistry and Physics*, 11, 7, 3067-3091, 2011.

555

556 Crewell, S. and Löhnert, U.: Accuracy of cloud liquid water path from ground-based microwave radiometry 2.
557 Sensor accuracy and synergy, *Radio Sci.*, 38, 8042, doi: 10.1029/2002RS002634, 2003.

558 Delanoe, J. and Hogan, R. J.: A variational scheme for retrieving ice cloud properties from combined radar,
559 lidar, and infrared radiometer, *J. Geophys. Res.-Atmos.*, 113, doi:10.1029/2007JD009000, 2008.

560 Fernández, A. J., Sicard, M., Costa, M. J., Guerrero-Rascado, J. L., Gómez-Amo, J. L., Molero, F., Barragán,
561 R., Bortoli, D., Bedoya-Velásquez, A. E., Utrillas, M. P., Salvador, P., Granados-Muñoz, M. J., Potes, M.,
562 Ortiz-Amezcuca, P., Martínez-Lozano, J. A., Artíñano, B., Muñoz-Porcar, C., Salgado, R., Román, R.,
563 Rocadenbosch, F., Salgueiro, V., Benavent-Oltra, J. A., Rodríguez-Gómez, A., Alados-Arboledas, L.,
564 Comerón, A., and Pujadas, M.: February 2017 extreme Saharandustoutbreak in theIberianPeninsula: fromlidar-
565 derivedopticalproperties to evaluation of forecastmodels, *Atmos. Chem. Phys. Discuss.*,
566 <https://doi.org/10.5194/acp-2018-370>, in review, 2018.

567

568 Granados-Muñoz, M.J, Navas-Guzmán, F., Bravo-Aranda, J. A., Guerrero-Rascado, J. L., Lyamani, H.,
569 Valenzuela, A., Titos, G., Fernández-Gálvez, J., and Alados-Arboledas, L.: hygroscopic growth of atmospheric
570 aerosol particles based on active remote sensing and radiosounding measurements: selected cases in
571 southeastern Spain. *Atmos. Meas. Tech.*, 8, 705–718, 2015.

572

573 Granados-Muñoz, M.J., Bravo-Aranda, J.A., Baumgardner, D., Guerrero-Rascado, J.L., Pérez-Ramírez, D.,
574 Navas-Guzmán, F., Veselovskii, I., Lyamani, H., Valenzuela, A., Olmo, F.J., Titos, G., Andrey, J., Chaikovsky,
575 A., Dubovik, O., Gil-Ojeda, M., Alados-Arboledas, L.: A comparative study of aerosol microphysical properties
576 retrieved from ground-based remote sensing and aircraft in situ measurements during a Saharan dust event.
577 *Atmospheric Measurement Techniques* 9, 3, 1113-1133, 2016.

578

579 Guerrero-Rascado, J.L., Ruiz, B., Alados-Arboledas, L.: Multi-spectral Lidar characterization of the vertical
580 structure of Saharan dust aerosol over southern Spain. *Atmospheric Environment* Volume 42, Issue 11, 2668-
581 268, 2008a.

582

583 Guerrero-Rascado, J.L., Ruiz, B., Chourdakis, G., Georgoussis, G., and Alados-Arboledas, L.: One year of
584 water vapour Raman lidar measurements at the Andalusian Centre for Environmental Studies (CEAMA), Int.
585 *J. Remote Sens.*, 29, 5437–5453, 2008b.

586 Holzworth, C. G. Estimates of mean maximum mixing depths in the contiguous United States. *Monthly Weather*
587 *Review*, 92, 235–242, 1964.

588 Holben, B. N., Eck, T. F., Slutsker, I., Tanre, D., Buis, J. P., Setzer, A., Vermote, E., Reagan, J.A., Kaufman,
589 Y. J., Nakajima, T., Lavenus, F., Jankowiak, I., and Smirnov, A.: AERONET –A Federated Instrument Network
590 and Data Archive for Aerosol Characterization, *Remote Sens. Environ.*, 66, 1–16, 1998.

591

592 Kiehl, J. and Trenberth, K. E.: Earth’s annual global mean energy budget, *B. Am. Meteorol. Soc.*, 78, 197–
593 208, 1997.

594

595 Löhnert, U. and Crewell, S.: Accuracy of cloud liquid water path from ground-based microwave radiometry 1.
596 Dependency on cloud model statistics, *Radio Sci.*, 38, 8041, doi: 10.1029/2002RS002654, 2003.

597

598 Löhnert, U. and Maier, O.: Operational profiling of temperature using ground-based microwave radiometry at
599 Payerne: prospects and challenges, *Atmos. Meas. Tech.*, 5, 1121–1134, doi: 10.5194/amt-5-1121-2012, 2012.

600

601 Löhnert, U., Crewell, S., and Simmer, C.: An integrated approach toward retrieving physically consistent
602 profiles of temperature, humidity, and cloud liquid water, *J. Appl. Meteorol.*, 43, 1295–1307, 2004.

603

604 Löhnert, U., Turner, D. D., and Crewell, S.: Ground-Based Temperature and Humidity Profiling Using Spectral
605 Infrared and Microwave Observations. Part I: Simulated Retrieval Performance in Clear-Sky Conditions,
606 *Journal of Applied Meteorology and Climatology*, 48, 1017–1032, doi:10.1175/2008JAMC2060.1, 2009.

607
608 Lyamani, H., Olmo, F. J., Alcántara, A., and Alados-Arboledas, L.: Atmospheric aerosols during the 2003 heat
609 wave in southeastern Spain I: Spectral optical depth, *Atmos. Environ.*, 40, 6453–6464, 2006a.
610
611 Lyamani, H., Olmo, F. J., Alcántara, A., and Alados-Arboledas, L.: Atmospheric aerosols during the 2003 heat
612 wave in southeastern Spain II: microphysical columnar properties and radiative forcing, *Atmos. Environ.*, 40,
613 6465–6476, 2006b.
614
615 Lyamani, H., Olmo, F. J., and Alados-Arboledas, L.: Physical and optical properties of aerosols over an urban
616 location in Spain: seasonal and diurnal variability, *Atmos. Chem. Phys.*, 10, 239–254, doi: 10.5194/acp-10-239-
617 2010, 2010.
618
619 Lyamani, H., Fernández-Gálvez, J., Valenzuela, A., Antón, M., Alados, I., Titos, G., Olmo, F.J.: Aerosol
620 properties over two urban sites in South Spain during an extended stagnation episode in winter season.
621 *Atmospheric Environment*, 62, 424-432, 2012.
622
623 Maschwitz, G., Löhnert, U., Crewell, S., Rose, T., and Turner, D. D.: Investigation of ground based microwave
624 radiometer calibration techniques at 530 hPa, *Atmospheric Measurement Techniques*, 6, 2641–2658, doi:
625 10.5194/amt-6-2641-2013, 2013.
626 Mattis, I., Ansmann, A., Althausen, D., Jaenisch, V., Wandinger, U., Müller, D., Arshinov, Y. F., Bobrovnikov,
627 S. M., and Serikov, I. B.: Relative-humidity profiling in the troposphere with a Raman lidar, *Appl. Optics*, 41,
628 6451–6462, 2002.
629 Moreira, G. de A., Guerrero-Rascado, J. L., Bravo-Aranda, J. A., Benavent-Oltra, J. A., Ortiz-Amezcuca, P.,
630 Román, R., Bedoya-Velásquez, A. E., Landulfo, E., and Alados-Arboledas, L. Study of the planetary boundary
631 layer by microwave radiometer, elastic lidar and Doppler lidar estimations in Southern Iberian Peninsula,
632 *Atmospheric research*, <https://doi.org/10.1016/j.atmosres.2018.06.007>, 213, 185-195, 2018.
633
634 Navas-Guzmán, F., Bravo-Aranda, J.A., Guerrero-Rascado, J.L., Granados-Muñoz, M.J, and Alados-Arboledas,
635 L.: Statistical analysis of aerosol optical properties retrieved by Raman lidar over Southeastern Spain. *Tellus*
636 *B*, 65, 21234, 2013.
637
638 Navas-Guzmán, F., Fernández-Gálvez, J., Granados-Muñoz, M.J, Guerrero-Rascado, J.L., Bravo-Aranda, J.A.,
639 and Alados-Arboledas, L.: Tropospheric water vapour and relative humidity profiles from lidar and microwave
640 radiometry. *Atmos. Meas. Tech.*, 7, 1201-1211, 2014a.

641 Navas-Guzmán, F., O. Stähli, and N. Kämpfer: An integrated approach toward the incorporation of clouds in
642 the temperature retrievals from microwave measurements, *Atmos. Meas. Tech.*, 7, 1619-1628,
643 doi:10.5194/amt-7-1619-2014, 2014b.

644 Navas-Guzmán, F., N. Kämpfer, and A. Haeferle: Validation of brightness and physical temperature from two
645 scanning microwave radiometers in the 60 GHz O₂ band using radiosonde measurements, *Atmos. Meas. Tech.*,
646 9, 4587-4600, 2016.

647 Navas-Guzmán, F., N. Kämpfer, F. Schranz, W. Steinbrecht, and A. Haeferle: Intercomparison of stratospheric
648 temperature profiles from a ground-based microwave radiometer with other techniques, *Atmos. Chem. Phys.*,
649 17, 14085-14104, <https://doi.org/10.5194/acp-17-14085-2017>, 2017.

650 Ortiz-Amezcuca, P., Guerrero-Rascado, J. L., Granados-Muñoz, M. J., Bravo-Aranda, J. A., and Alados-
651 Arboledas, L.: Characterization of atmospheric aerosols for a long range transport of biomass burning particles
652 from Canadian forest fires over the southern Iberian Peninsula in July 2013, *Óptica Pura y Aplicada*, 47, 43–
653 49, 2014.

654 Ortiz-Amezcuca, P., Guerrero-Rascado, J. L., Granados-Muñoz, M. J., Benavent-Oltra, J. A., Böckmann, C.,
655 Samaras, S., Stachlewska, I. S., Janicka, L., Baars, H., Bohlmann, S., and Alados-Arboledas, L.: Microphysical
656 characterization of long-range transported biomass burning particles from North America at three EARLINET
657 stations, *Atmos. Chem. Phys.*, 17, 5931–5946, <https://doi.org/10.5194/acp-17-5931-2017>, 2017.

658

659 O'Connor, E. J., Illingworth, A. J., Brooks, I. M., Westbrook, C. D., Hogan, R. J., Davies, F., Brooks, B. J.: A
660 method for estimating the turbulent kinetic energy dissipation rate from a vertically-pointing Doppler lidar, and
661 independent evaluation from balloon-borne in-situ measurements. *Journal of Atmospheric and Oceanic*
662 *Technology*, v. 27, n. 10, 1652-1664, 2010.

663 Río, S., Herrero, L., Pinto-Gomes, C., Penas, A.: Spatial analysis of mean temperature trends in Spain over the
664 period 1961–2006, *Global and Planetary Change*, Volume 78, Issues 1–2, Pages 65-75, ISSN 0921-
665 8181, <https://doi.org/10.1016/j.gloplacha.2011.05.012>, 2011.

666 Rodgers, C.: *Inverse Methods for Atmospheric Sounding: Theory and Practice*, World Scientific Publishing
667 Company, Incorporated, Singapore, 2000.

668 Román, R., Antón, M., Cazorla, A., Miguel, A. D., Olmo, F. J., Bilbao, J., Alados-Arboledas, L.: Calibration
669 of an all-sky camera for obtaining sky radiance at three wavelengths, *Atmos. Meas. Tech.*, 5, 2013–
670 2024, doi:10.5194/amt-5-2013-2012, 2012.

671 Román, R., Cazorla, A., Toledano, C., Olmo, F.J., Cachorro, V.E., de Frutos, A., Alados-Arboledas, L.: Cloud
672 cover detection combining high dynamic range sky images and ceilometer measurements. *Atmospheric*
673 *research*, 196, 224-236, <http://dx.doi.org/10.1016/j.atmosres.2017.06.006>, 2017a.

674 Román, R., Torres, B., Fuertes, D., Cachorro, V.E., Dubovik, O., Toledano, C., Cazorla, A., Barreto, A., Bosch,
675 J.L., Lapyonok, T., González, R., Goloub, P., Perrone, M.P., Olmo, F.J., de Frutos, A., Alados-Arboledas, L.:
676 Remote sensing of lunar aureole with a sky camera: Adding information in the nocturnal retrieval of aerosol
677 properties with GRASP code. *Remote Sensing of Environment*, 196, 238-252,
678 <http://dx.doi.org/10.1016/j.rse.2017.05.013>, 2017b.

679 Rose, T., S. Crewell, U. Löhnert, C. Simmer.: A network suitable microwave radiometer for operational
680 monitoring of the cloudy atmosphere. *Atmospheric Research*, Vol.75, No.3, 183-200, 2005.

681

682 Stankov, B. B.: Multisensor Retrieval of Atmospheric Properties, *B. Am.Meteorol. Soc.*, 79, 1835–1854, doi:
683 [10.1175/1520-0477\(1998\)079<1835:MROAP>2.0.CO;2](https://doi.org/10.1175/1520-0477(1998)079<1835:MROAP>2.0.CO;2), 1998.

684 Stevens, B. and Bony, S.: Water in the atmosphere, *Phys. Today*, 66, p. 29, doi:10.1063/PT.3.2009, 2013.

685 Stull, R. B. *An Introduction to Boundary Layer Meteorology*. vol. 13, Kluwer Academic Publishers, the
686 Netherlands, Dordrecht/Boston/London, 1988.

687 Stull, R. B. *Meteorology for Scientists and Engineers*. 3rd Edition, Uni. Of British Columbia, 2011.

688 Titos, G., del Águila A., Cazorla, A., Lyamani, H., Casquero-Vera, J.A., Colombi, C., Cuccia, E., Gianelle, V.,
689 Alastuey, A., Alados-Arboledas, L.: Spatial and temporal variability of carbonaceous aerosols: assessing the
690 impact of biomass burning in the urban environment. *Science of the Total Environmental*, 578: 613-625,
691 <http://hdl.handle.net/10481/47096>, 2017.

692

693 Titos, G., Foyo-Moreno, I., Lyamani, H., Querol, X., Alastuey, A., and Alados-Arboledas, L.: Optical properties
694 and chemical composition of aerosol particles at an urban location: An estimation of the aerosol mass scattering
695 and absorption efficiencies, *J. Geophys.Res.-Atmos.*, 117, D04206, doi:10.1029/2011JD016671, 2012.

696

697 Turner, D. D., Clough, S. A., Liljegren, J. C., Clothiaux, E. E., Cady-Pereira, K. E., and Gaustad, K. L.:
698 Retrieving Liquid Water Path and Precipitable Water Vapor From the Atmospheric Radiation Measurement
699 (ARM) Microwave Radiometers, *IEEE Transactions on Geoscience and Remote Sensing*, 45, 3680–3690,
700 doi:10.1109/TGRS.2007.903703, 2007.

701

702 Valenzuela, A., Olmo, F.J., Lyamani, H., Granados-Muñoz, M.J., Antón, M., Guerrero-Rascado, J.L.,
703 Quirantes, A., Toledano, C., Perez-Ramírez, D., Alados-Arboledas, L.: Aerosol transport over the western
704 mediterranean basin: Evidence of the contribution of fine particles to desert dust plumes over Alborán island.
705 *Journal of Geophysical Research*, 119, 24, 14,028-14,044, 2014.

706

707 Vaughan, G., Wareing, D., Thomas, L., and Mitev, V.: Humidity measurements in the free troposphere using
708 Raman backscatter, *Q. J. Roy. Meteorol. Soc.*, 114, 1471–1484, 1988.

709 Vogelmann, A. M., McFarquhar, G. M., Ogren, J. A., Turner, D. D., Comstock, J. M., Feingold, G., Long,
710 C. N., Jonsson, H. H., Bucholtz, A., Collins, D. R., Diskin, G. S., Gerber, H., Lawson, R. P., Woods, R.
711 K., Andrews, E., Yang, H., Chiu, J. C., Hartsock, D., Hubbe, J. M., Lo, C., Marshak, A. J. W., S. A., M.,
712 and Toto, T.: RACORO.: extended-term aircraft observations of boundary layer clouds, Bull. Am. Meteorol.
713 Soc., 93, 861–878, doi:10.1175/BAMS-D-11-00189.1, 2012.

714

715 **Figure captions**

716 **Figure 1.** Mean bias (solid line) and standard deviation (dashed line) on all-weather conditions (AWC, blue)
717 and cloud-free conditions (CFC, red) for temperature (a) and RH (b) profiles between RS and MWR.

718

719 **Figure 2.** IWV from MWR versus RS for all-weather conditions (AWC, in blue) and cloud-free conditions
720 (CFC, in red). The gray dashed-line refers to 1:1 line.

721

722 **Figure 3.** Mean bias (solid line) and standard deviation (dashed line) on daytime (red) and night-time (blue) for
723 T (a) and RH (b) profiles between MWR and RS, all for cloud-free conditions (CFC).

724

725 **Figure 4.** Mean 24-h cycle for temperature profiles and ABLH by season and year. The magenta line refers to
726 the mean $ABLH^{\max}$ and the white contour is the SD.

727

728 **Figure 5.** Mean 24-h cycle for RH profiles and ABLH by season and year. The magenta line refers to the
729 mean $ABLH^{\max}$ and the white contour is the SD.

730

731 **Figure 6.** Seasonal boxplots of temperature presented for nine atmospheric volumes covering the 39 bins of the
732 MWR for the years 2012 (red), 2013 (green), 2014 (blue), 2015 (black) and 2016 (cyan). Winter (panel a),
733 spring (panel b), summer (panel c), and autumn (panel d). In the boxes are represented the 25 and 75 percentile,
734 the median, the maximum and minimum, and the outliers marked with asterisks.

735

736 **Figure 7.** Seasonal boxplots of RH presented for nine atmospheric volumes covering the 39 bins of the MWR
737 for the years 2012 (red), 2013 (green), 2014 (blue), 2015 (black) and 2016 (cyan). Winter (panel a), spring
738 (panel b) summer (panel c) and autumn (panel d). In the boxes are represented the 25 and 75 percentile, the
739 median, the maximum and minimum, and the outliers marked with asterisks

740

741 **Figure 8.** Seasonal boxplots of IWV the years 2012 (red), 2013 (green), 2014 (blue), 2015 (black) and 2016
 742 (cyan). The line within the box refers to the median value, and the top and bottom of the box are the 75 and 25
 743 quartiles, respectively. The outliers are marked with a red cross symbol.

744

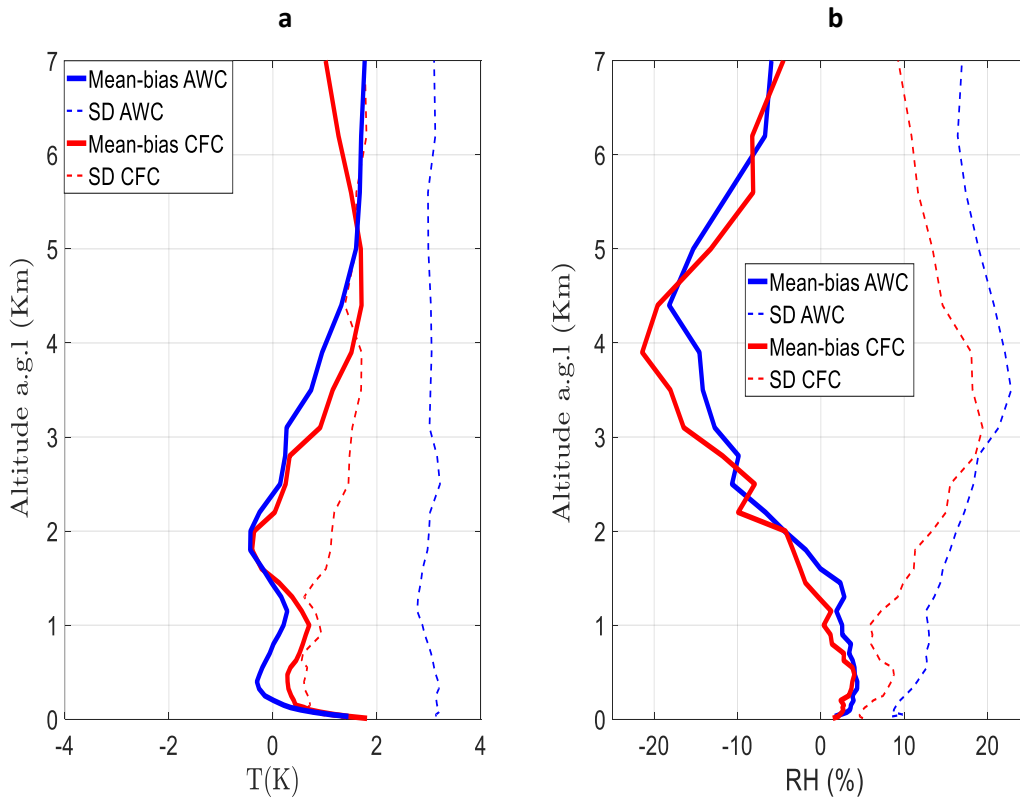
745 **Table captions**

746 **Table 1.** MWR measurements over five-years at Granada station, reporting for each year the total of days (D)
 747 and profiles (P) measured by month.

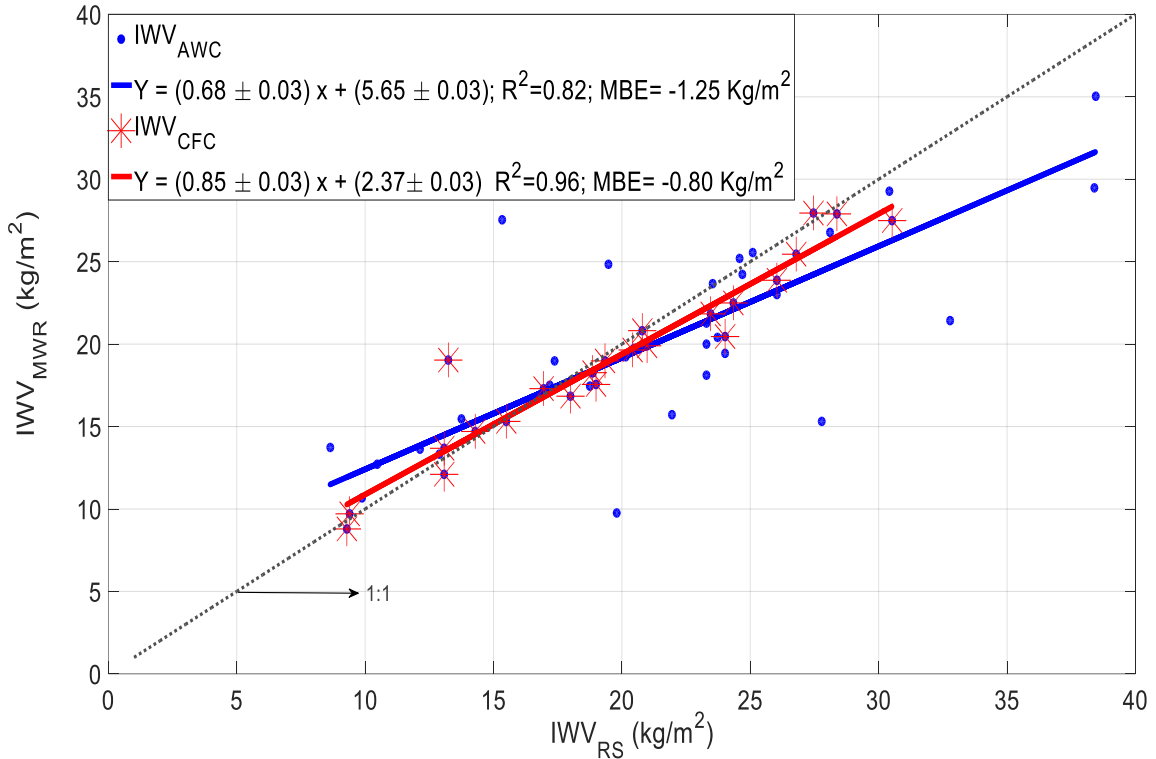
748 **Table 2.** Inter-annual trends of temperature and RH by season and height-range. Where W (winter), S (spring),
 749 SU (summer) and A (autumn).

750 **Table 3.** Inter-annual trend of IWV and $IWV_{aeronet}$ by season in the period 2012-2016.

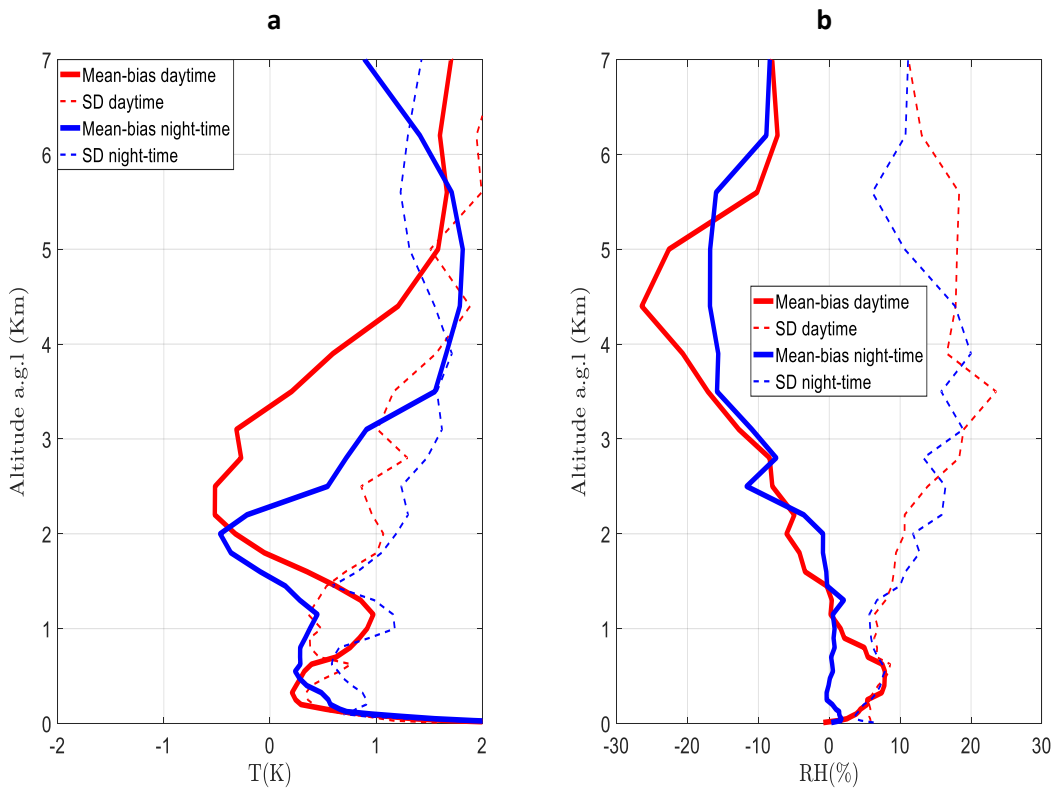
751



752



753
754
755



756

757

758

759

760

761

762

763

764

765

766

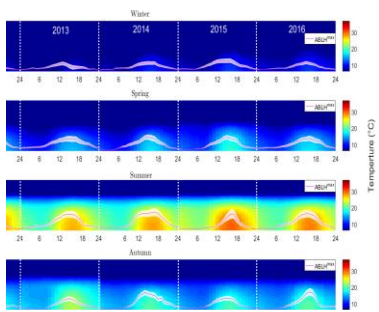
767

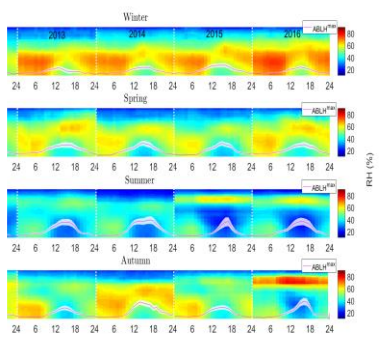
768

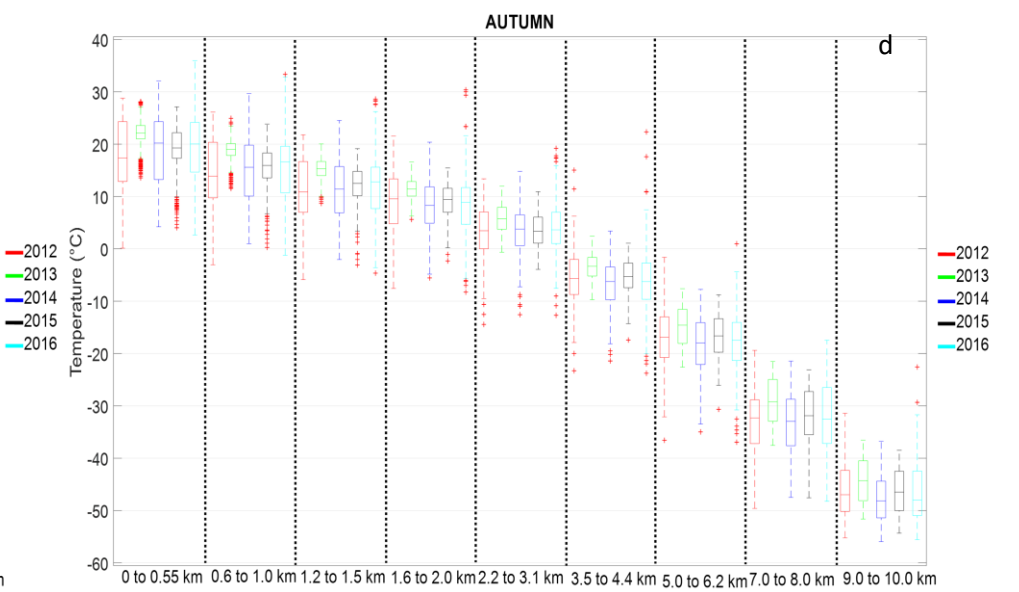
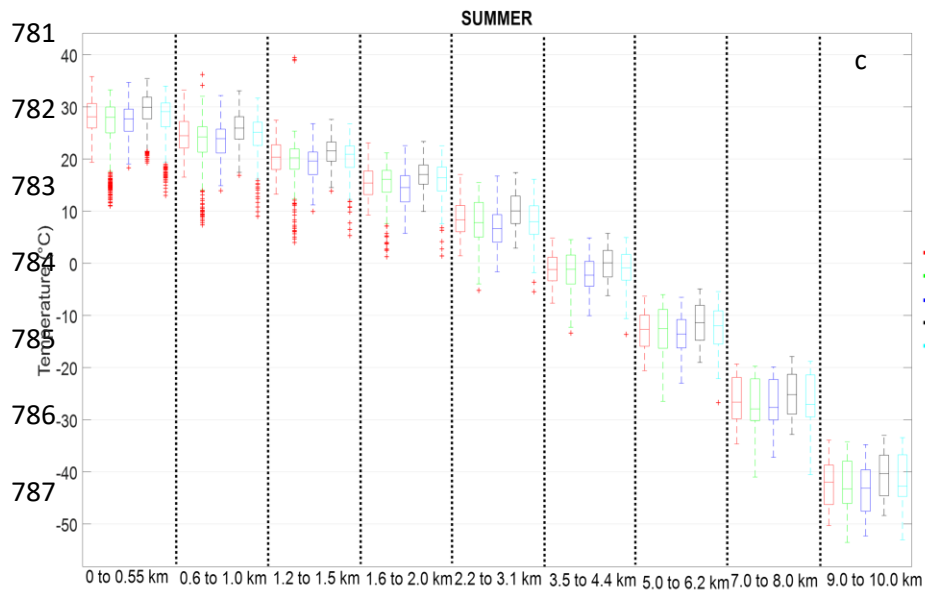
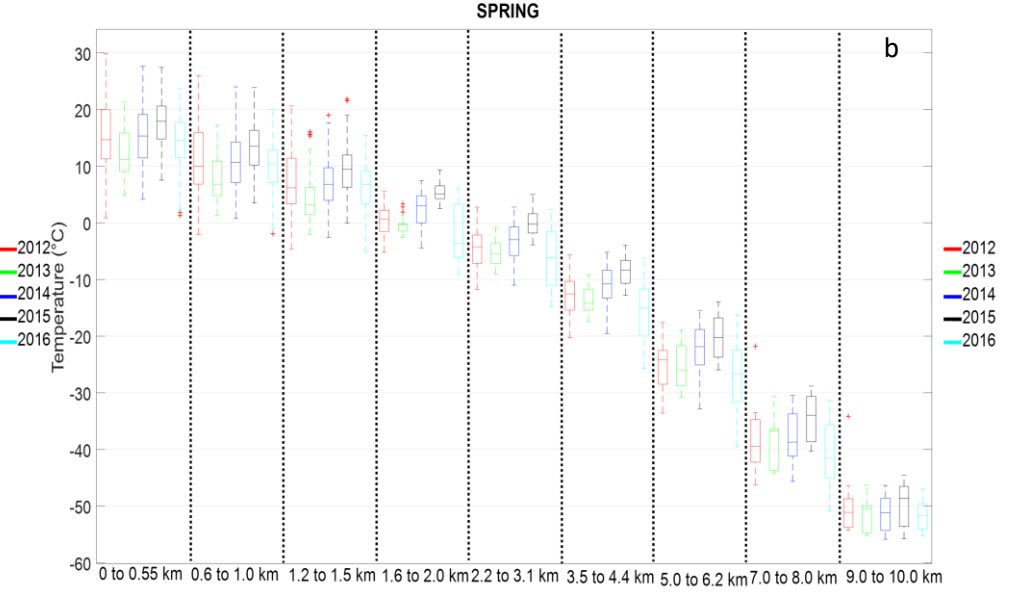
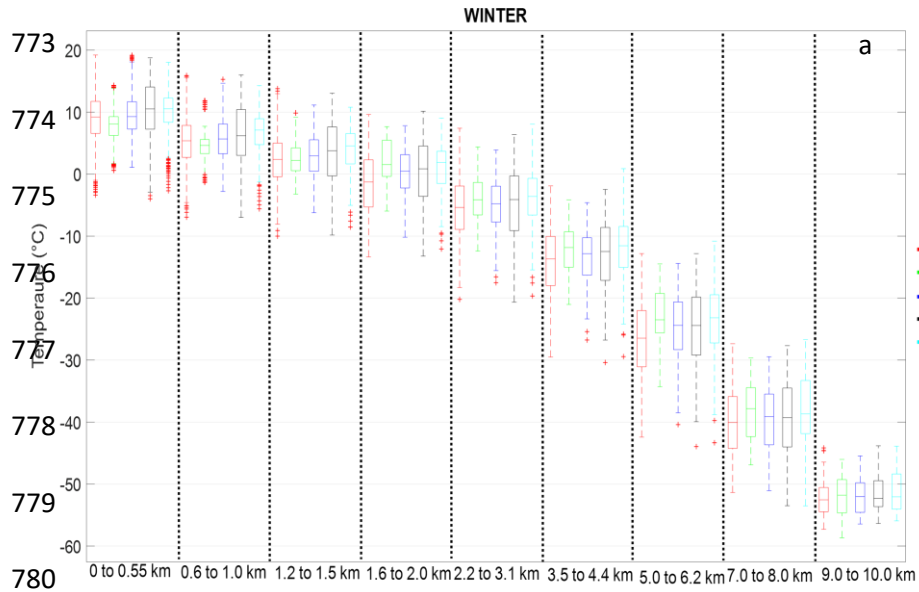
769

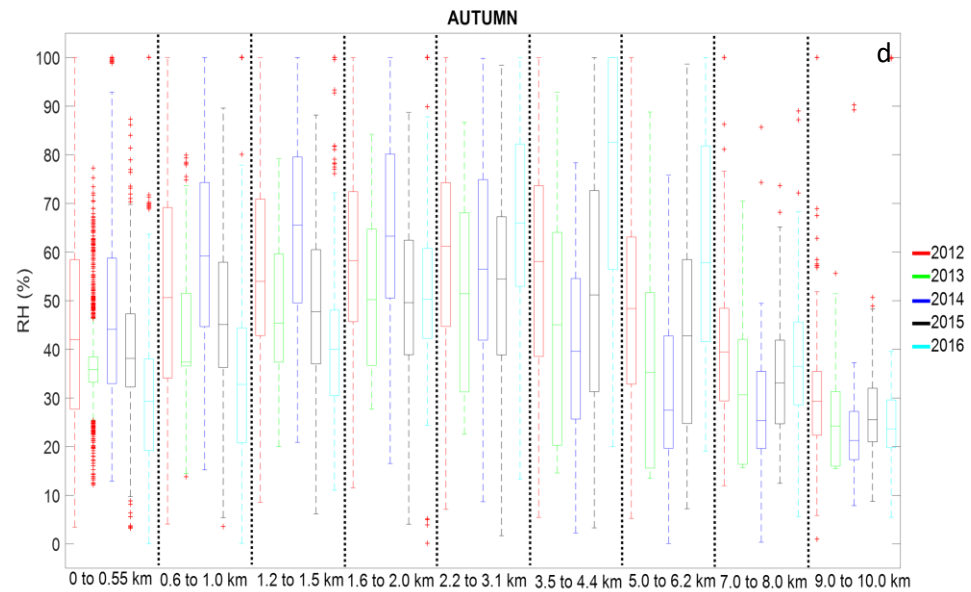
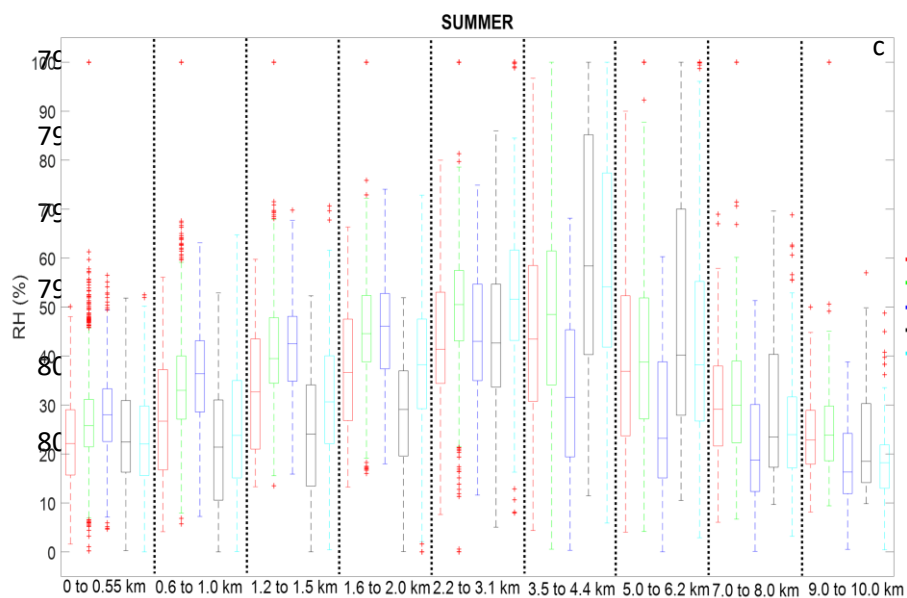
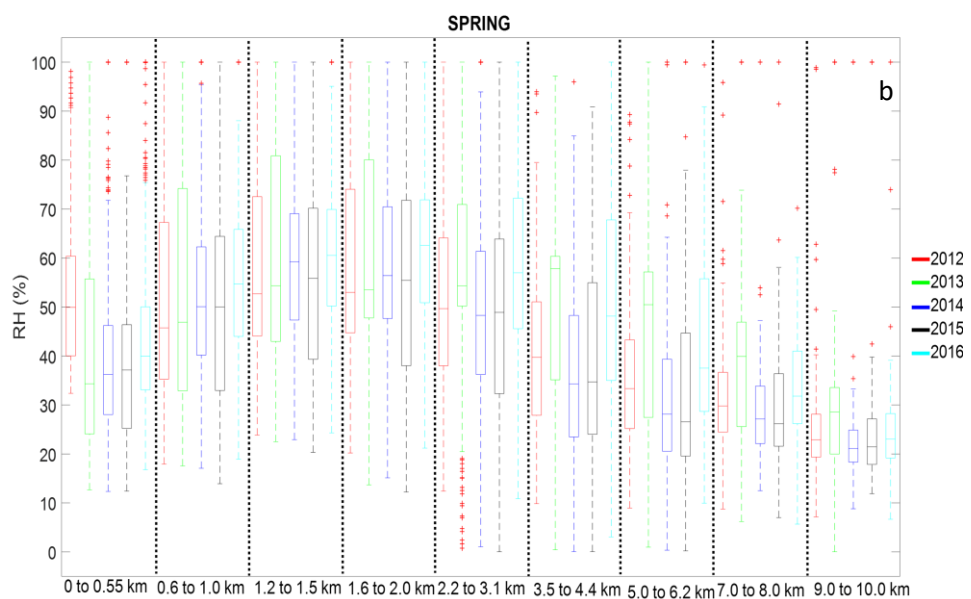
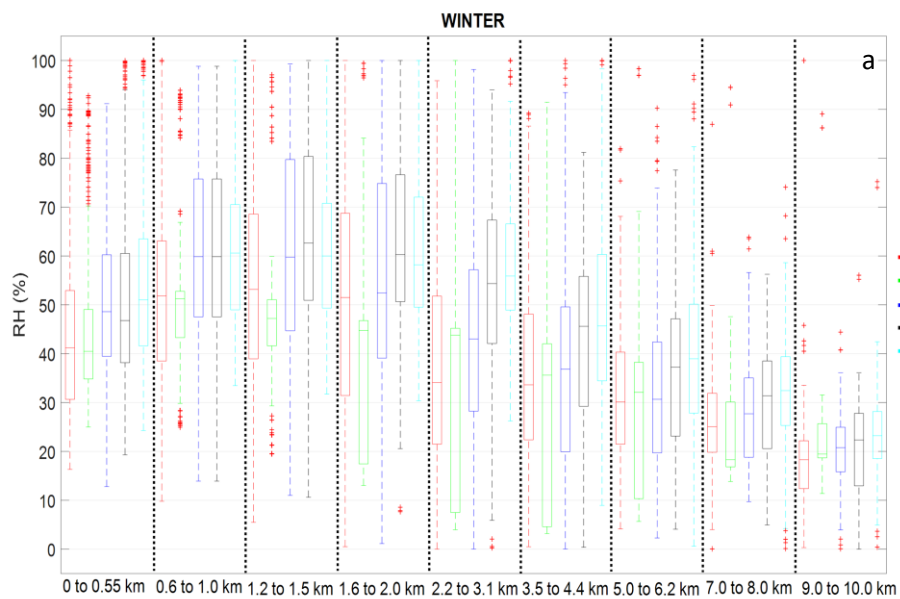
770

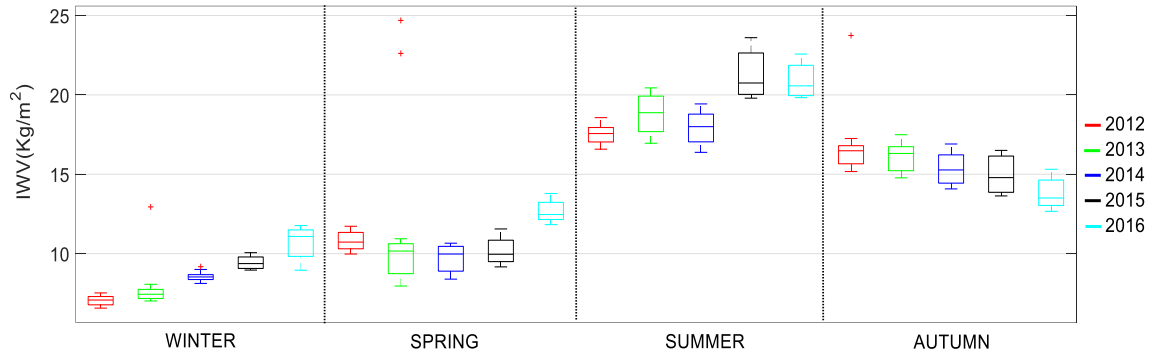
771











802

803

804

YEAR	2012		2013		2014		2015		2016	
MONTH	D	P	D	P	D	P	D	P	D	P
January	31	12648	31	12648	20	14400	5	3600	28	20160
February	29	11832	28	11424	28	20160	28	20160	29	20880
March	31	12648	31	12648	31	22320	31	22320	11	7920
April	30	12240	30	12240	11	7920	30	21600	26	18720
May	31	12648	8	5760	20	14400	16	11520	31	22320
June	30	12240	30	21600	30	21600	0	0	24	17280
July	31	12648	31	22320	21	15120	18	12960	31	22320
August	31	12648	31	22320	31	22320	31	22320	31	22320
September	30	12240	30	21600	30	21600	30	21600	17	12240
October	31	12648	31	22320	16	11520	27	19440	31	22320
November	30	12240	24	17280	30	21600	30	21600	25	18000
December	31	12648	14	10080	15	10800	30	21600	0	0
TOTAL	366	149328	319	192240	283	203760	276	198720	284	204480

812

813

814

815

816

817

818

819

820

821		H1	H2	H3	H4	H5	H6	H7	H8	H9	
822	slope (°C/year)	0.5 ± 0.6	0.5± 0.5	0.6± 0.3	0.6± 0.5	0.4± 0.8	0.4± 0.8	0.6± 0.5	0.1± 1.8	0.1± 3.1	W
	R ²	0.60	0.73	0.90	0.52	0.70	0.50	0.50	0.06	0.06	
823 T (K)	slope (°C/year)	0.7± 0.3	0.8± 0.3	0.8± 0.3	-0.3± 0.3	0.1± 0.4	0.1± 0.3	0.1± 0.3	-0.2± 0.3	0.1± 0.8	S
	R ²	0.18	0.26	0.29	0.001	0.01	0.001	0.001	0.01	0.01	
824	slope (°C/year)	0.4± 0.7	0.3± 0.9	0.3± 1.1	0.3± 0.8	0.2± 0.7	0.2± 1.0	0.3± 1.0	0.2± 0.8	0.1± 0.7	SU
	R ²	0.44	0.36	0.28	0.22	0.001	0.12	0.24	0.01	0.03	
826	slope (°C/year)	0.3± 0.5	0.4± 0.4	0.1± 0.5	-0.3± 0.7	-0.2± 0.7	-0.3± 0.7	-0.3± 0.6	-0.3± 0.6	-0.4± 0.5	A
	R ²	0.01	0.08	0.01	0.20	0.10	0.16	0.15	0.11	0.18	
827	slope (%/year)	2.6± 0.1	2.6± 0.1	2.9± 0.1	7.4± 0.1	5.42± 0.03	---	---	---	---	W
	R ²	0.79	0.77	0.54	0.56	0.91	---	---	---	---	
828	slope (%/year)	-1.7± 0.1	2.1± 0.1	1.7± 0.2	2.1± 0.1	0.9± 0.2	---	---	---	---	S
	R ²	0.19	0.91	0.68	0.76	0.15	---	---	---	---	
829 (%)	slope (%/year)	-0.4± 0.3	-1.7± 0.1	-2.0± 0.1	-1.2± 0.1	1.3± 0.2	---	---	---	---	SU
	R ²	0.04	0.19	0.18	0.08	0.17	---	---	---	---	
830	slope (%/year)	-2.3± 0.1	-2.8± 0.1	-2.6± 0.1	-1.7± 0.1	1.3± 0.2	---	---	---	---	A
	R ²	0.40	0.17	0.17	0.18	0.12	---	---	---	---	

832

833

	slope (kgm ⁻² /year)	R ²	Season
IWV _{MWR} (kgm ²)	1.0 ± 0.1	0.95	WINTER
	0.3 ± 0.7	0.26	SPRING
	0.8 ± 0.1	0.73	SUMMER
	-0.8 ± 0.2	0.95	AUTUMN
IWV _{aeronet} (cm)	0.07 ± 0.03	0.60	WINTER
	0.01 ± 0.05	0.02	SPRING
	0.03 ± 0.03	0.30	SUMMER
	-0.03 ± 0.04	0.20	AUTUMN